The International Journal of Advanced Manufacturing Technology (2025) 136:2623–2636
https://doi.org/10.1007/s00170-024-14935-4

ORIGINAL ARTICLE

The effect of hot corrosion on mechanical properties of the tin-doped titanium aluminide alloy

Steven Magogodi[1,3] · **Maria Ntsoaki Mathabathe**[1] · **Rirhandzu Rikhotso-Mbungela**[2] · **Velile Vilane**[5] · **Charles Siyasiya**[3] · **Amogelang Sylvester Bolokang**[1,4]

Received: 22 August 2024 / Accepted: 12 December 2024 / Published online: 10 January 2025
© The Author(s) 2025

Abstract

This work investigates the hot corrosion behaviour of Ti-48Al-2Nb-0.3Si and Ti-48Al-2Nb-0.3Si-1Sn alloys under 25 wt.% NaCl and 75 wt.% Na_2SO_4 molten salt mixture at 900 °C. The alloys were developed through vacuum arc melting and casting. The corrosion kinetics of the alloys were measured by mass change per unit surface area. The results revealed that both alloys experienced hot corrosion attacks; however, Ti-48Al-2Nb-0.3Si-1Sn alloy demonstrated superior corrosion resistance and retained good mechanical properties compared to the Ti-48Al-2Nb-0.3Si.

Keywords Ti-48Al-2Nb-0.3Si-1Sn · Hot corrosion · Oxides · Mechanical properties · Salts

1 Introduction

Titanium aluminides (TiAl) are materials of interest for high-temperature applications, particularly in aero-engines [1]. Such interest is due to their low density (3.7 ~ 4.2 g/cm^3), high-temperature strength, and good corrosion resistance at room temperature [1–3]. The performance of these alloys in resisting oxidation and corrosion at elevated temperatures contributes to positive industrialisation in engineering applications. These materials retain good oxidation resistance beneath 750 °C, and they are likely to replace Ni-based super-alloys owing to their weight reduction and promising mechanical properties [4–6]. However, they suffer inherent brittleness at room temperature and vulnerability to hot corrosion above 800 °C [2]. Improving room temperature ductility of the TiAl-based alloys is no longer a major concern, but rather the manufacturing remains a challenge due to high costs and complex post-processing requirements [7]. Previously, extensive efforts were made to enhance room temperature ductility and good high-temperature strength by employing methods such as micro-alloying of ternary, quaternary, and quinary TiAl-based alloys [8]. Furthermore, grain refinement using pre-alloyed powder metallurgy and heat treatment to achieve optimal phase distribution was investigated [7, 8, 10, 11]. Notably, several processes, including ingot metallurgy, investment casting, and powder metallurgy, were previously used to produce TiAl-based alloys [12–15]. Among these techniques, powder metallurgy is particularly suited for this purpose as it facilitates the formation of fine-grained microstructures, improved homogeneity in grain size, and proper phase distribution [12]. It also allows for the fabrication of precise components through near-net shaping technologies like cold pressing and sintering [16, 17]. Cold pressing technique reduces production costs by allowing the manufacture of complex shapes without the need for post-processing [18–20]. Vacuum arc re-melting (VAR) is a well-known melting technology used in the production of high-performance materials such as nickel-base alloys and employed in reactive metals such as

---

✉ Amogelang Sylvester Bolokang
sbolokang@csir.co.za

[1] Manufacturing Cluster, Council of Scientific Industrial Research, Meiring Naude Road, PO Box 395, Pretoria, South Africa

[2] Chemical Cluster, Nanostructured Materials Laboratory, Council of Scientific Industrial Research, Meiring Naude Road, PO Box 395, Pretoria, South Africa

[3] Department of Material Science and Metallurgical Engineering, Faculty of Engineering, Built Environment and Information Technology, University of Pretoria, Pretoria, South Africa

[4] Department of Physics, University of the Free State, P.O. Box 339, Bloemfontein 9300, ZA, South Africa

[5] Department of Physics, CHRTEM, Nelson Mandela University, Gqeberha 6001, South Africa

titanium and zirconium [21]. This manufacturing technique is useful for materials with high affinity to oxygen such as titanium and its alloys. Vacuum arc melting has proven to be useful in reaching this goal [22]. TiAl-based alloy components, such as high-performance exhaust valves, turbine wheels in turbocharged engines, and turbine blades in aerospace applications, often have service temperatures ranging between 600 and 950 °C [23, 24]. As a result, extensive research has been undertaken in recent years to improve the oxidation resistance of TiAl-based alloys at elevated temperatures ranging from 700 to 900 °C. Remarkable results have been achieved through elemental alloying of Nb, Si, Sn, W, and Cr [25–28]. The effect of Si alloying to TiAl-based alloys promotes titanium silicide (Ti_5Si_3), which stimulates elevated temperature strength and forms a surface silica layer (SiO_2) that reduces the oxidation by slowing down the oxygen diffusion into the material [29, 30]. The addition of Sn likewise improves the oxidation resistance by enhancing alumina (Al_2O_3) formation on the surface of the TiAl-based alloys [31–33]. Pan et al. [33] reported that the inclusion of Sn in TiAl alloys promotes superior oxidation resistance owing to the presence of Al_2O_3 and SnO_2 oxides. However, the oxidation resistance of these materials is often compromised due to the presence of impurities in their in-service environment, such as NaCl from the marine atmosphere, sulphur from fuel, and moisture accumulation on the surface of TiAl components [2, 6]. Therefore, it is crucial for TiAl alloys to exhibit high resistance to oxidation and hot corrosion at elevated temperatures. Hot corrosion in metallic materials refers to the degradation caused by the interaction with fused salts at high temperatures [34]. The exposure of TiAl-based alloys to salt deposits at high temperatures accelerates oxidation and leads to the degradation of their protective scale [34, 35], resulting in the formation of surface porosity and premature fracture. Zhang et al. [36] conducted a comprehensive study on hot corrosion experiments, discovering that a higher concentration of aluminium greatly influenced the formation of a protective Al-rich oxide scale, resulting in reduced corrosion. Conversely, the growth of non-protective TiO_2 oxide scales on the surface of TiAl-based alloys accelerated their oxidation resistance above 800 °C, while the growth rate of the protective Al_2O_3 oxide scale was found to be slow [2]. They suffer inherent brittleness at room temperature and vulnerability to hot corrosion above 800 °C. Considering the significance of hot corrosion in the application of TiAl-based alloys, it is imperative to further investigate this phenomenon under presence of Sn. A notable research gap exists regarding the hot corrosion behaviour of Ti–Al intermetallic alloys alloyed with both Si and Sn alloying for extreme temperatures. The current work investigates the effect of hot corrosion on mechanical properties of Ti-48Al-2Nb-0.3Si and Ti-48Al-2Nb-0.3Si-1Sn melted alloys. These alloys were exposed under 25 wt.% NaCl and 75 wt.% Na_2SO_4 molten salt mixture at 900 °C to simulate their performance at elevated temperatures. TiAl-based materials have shown to suffer inherent brittleness at room temperature and vulnerability to hot corrosion above 800 °C [2]. The current results will give an indication of whether Sn improves the hot corrosion resistance at elevated temperature to assist in the design for the future of the alloys.

2 Experimental procedure

2.1 Alloy preparation

The Ti-48Al-2Nb-0.3Si/1Sn alloys were fabricated by cold pressing and melting. Table 1 shows the alloy compositions of pure Ti, Al, Nb, Sn, and Si metallic powders. Their mixed/blended powders were compacted using uniaxial cold pressing at 250 Bar using a 51-mm diameter cylindrical die. An electric vacuum arc furnace was used to melt the compacts under argon atmosphere. The melted buttons were machined into $12 \times 12 \times 2$ mm^3 specimens for corrosion testing using wire cutting. The specimens were solution treated at 1250 °C for 2 h before cooling in the furnace under an argon atmosphere. The Ti-48Al-2Nb-0.3Si/1Sn alloy fabrication is illustrated in Fig. 1.

2.2 Hot corrosion test

Three specimens were prepared for corrosion tests. The mass of each specimen was measured before and after the corrosion test. The cyclic hot corrosion behaviour was investigated under a molten salt mixture of Na_2SO_4 and 25 wt.% NaCl at 900 °C for ten cycles up to 60 h in the air. The salt mixture was dissolved in deionised water to form a saturated aqueous solution [35]. Followed by placing the specimen on the hot plate at 250 °C, the surfaces of the samples were sprayed with a saturated salt mixture to coat and evaporate the moisture [37]. The samples were weighed using an electronic mass balance to ensure a surface coating of 2 mg/cm^2. The sensitivity of the weighing balance used for the study was 10^{-4} g. The coated samples were placed in an alumina crucible and put inside a tubular high-temperature furnace and heated up to 900 °C. For every 6 h, the samples were withdrawn from the furnace, cooled in air, and taken for visible inspections. After each cycle, samples were

Table 1 The Ti-48Al-2Nb-0.3Si/1Sn alloys chemical compositions (at. %)

Elements	Ti	Al	Nb	Si	Sn
Ti–Al-Nb-Si	49.7	48	2	0.3	-
Ti–Al-Nb-Sn-Si	48.7	48	2	0.3	1

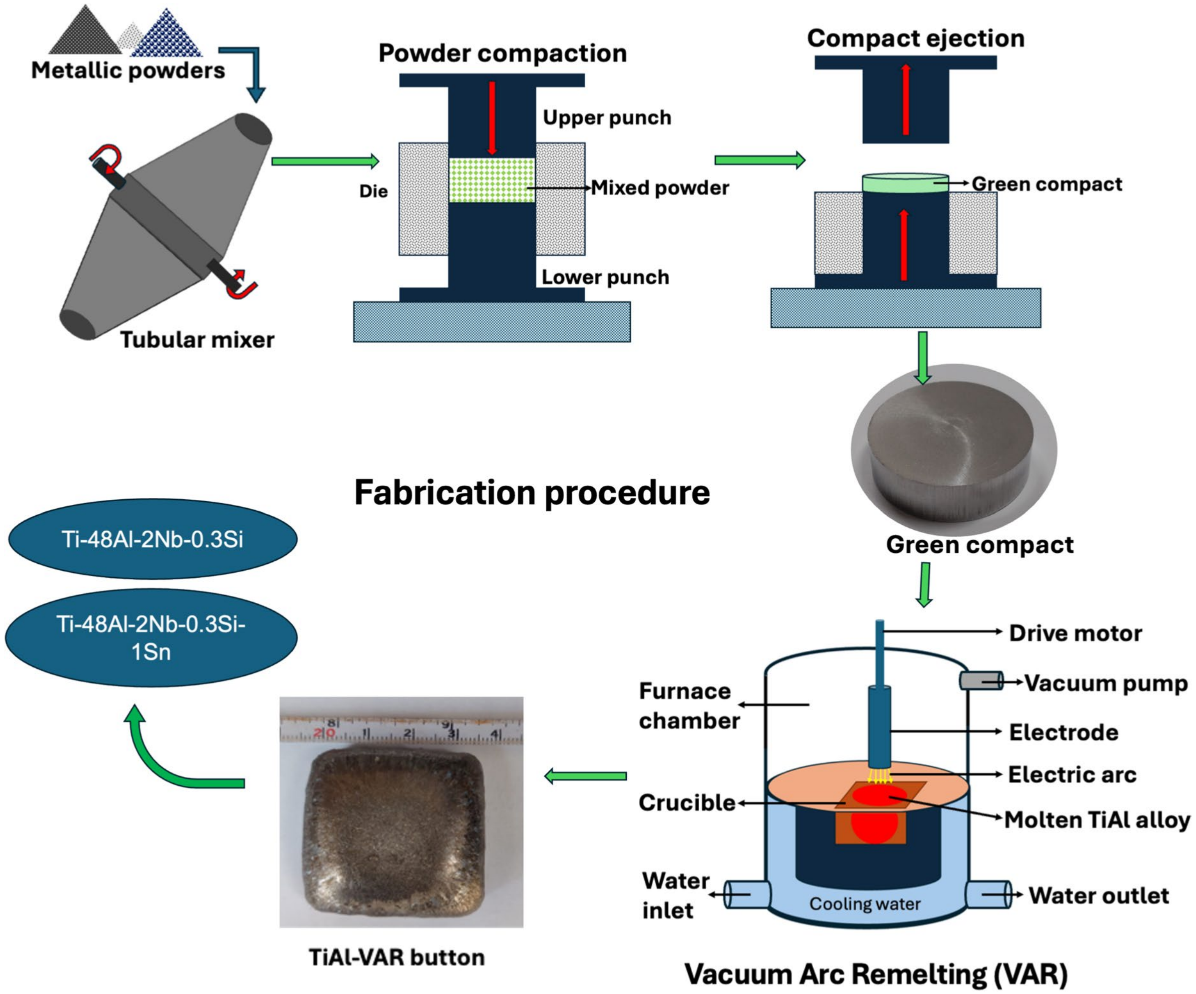

Fig. 1 The schematic diagram of the Ti-48Al-2Nb-0.3Si/1Sn alloy fabrication procedure

ultrasonically cleaned for 15 min and then cleaned with hot distilled water at ~ 80 °C using a soft brush to remove any loose particles left on the surface and dried using a hot plate [6]. The mass change was measured to establish the corrosion kinetics. Before returning the samples to the furnace, they were coated again with the saturated salt solution to maintain a constant concentration of corrosive agent on the surface of the samples. The process was repeated until the completion of 10 cycles. For corrosion kinetics measurements, the specimens were initially weighed before the corrosion tests to establish a baseline. After each corrosion cycle, the specimens were cooled, ultrasonically cleaned, brushed, dried, and weighed again to measure any changes in mass.

2.3 Sample characterisation

Before hot corrosion, samples were ground up to 1200 SiC grit finish and washed using deionised water and acetone for drying before the hot corrosion test. The Archimedes method was performed to determine the relative density of the produced samples. The VAR melted alloys were heat treated at 1250 °C for 2 h using a tube furnace under an argon-rich atmosphere. The furnace temperature was ramped at 20 °C/min from room temperature up to 1250 °C and held for 1 h before cooling down to room temperature within the furnace. To determine the mechanical properties, a profilometry-based indentation plastometer technique was used. The testing method resembles the ones in ref. [38].

The microhardness property of the fabricated Ti-48Al-2Nb-0.3Si/1Sn alloys was performed using the FUTURE-TECH FM-700 micro-hardness tester. The load of 500 gf ($HV_{0.5}$) was applied on the surface of the sample for indentation with a dwell time of 10 s, and the diagonal indent was separated by a spacing of 500 µm for ten points and the average was recorded. For microstructural observations, the samples were electro-polished and etched with Kroll's reagent. The used electrolytic solution was made of 600 ml methanol, 360 tetra-butanol, and 60 ml perchloric acid [39, 40]. The microstructures and surface morphologies of the phases and hot corrosion products were observed using optical microscopy and scanning electron microscopy (SEM) equipped with energy dispersion spectroscopy (EDS) which was used to study the elemental composition. The phases and structural development of the samples before and after the oxidation and hot corrosion were done by XRD using CuKα radiation in (2θ) angle range of 20–90°. The weight change per unit area (ΔW) of the samples after every hot corrosion test was calculated as Eq. 1 [2]:

$$\Delta W = \frac{\Delta M}{A} = \frac{m_i - m_o}{A} \tag{1}$$

where ΔW is the weight change per unit area (mg/cm^2), m_i is the mass of the corroded after a cycle (mg), m_o is the initial mass before any corrosion (mg), and A is the sample surface area in cm^2. Transmission electron microscopy (TEM) was used to analyse the oxide and scale formation. The scaling was dispersed in ethanol to create a dilute solution. This solution was then sonicated for 20 min at room temperature using an ultrasonic cleaner. After sonication, the solution was applied to a carbon-coated copper grid and left to dry. The prepared grid was subsequently loaded into a JEOL JEM 2100 high-resolution transmission electron microscope (HR-TEM) for analysis. Elemental composition was determined using an EDS detector from Thermo Fisher.

3 Results and discussion

3.1 Microstructures and phase composition

The microstructural features of the Ti-48Al-2Nb-0.3Si and Ti-48Al-2Nb-0.3Si-1Sn alloys prepared through vacuum arc melting are displayed in Fig. 2. The microstructures were homogenised at 1250 °C for 2 h. Both alloys exhibit lamellar microstructures consisting predominantly of α_2-Ti$_3$Al/γ-TiAl as evidenced by Clemens et al. [21]. The γ-TiAl phase is represented by the light grey regions, characterised by a face-cantered tetragonal L10 structure, while the α_2-Ti$_3$Al phase is indicated by the dark grey areas, characterised by a hexagonal close-packed DO$_{19}$ structure. The incorporation of Sn into TiAl-based alloys is reported to improve the alloy properties [41, 42]. The colonies with alternating light and dark grey phases result in a distinct lamellar arrangement. The colony boundaries of the Ti-48Al-2Nb-0.3Si/1Sn alloys display an irregular, serrated pattern, suggesting the presence of local structural variations or strain-induced deformations. The Ti-48Al-2Nb-0.3Si alloy shown in Fig. 2a has elongated lamellar colonies. In contrast, the Ti-48Al-2Nb-0.3Si-1Sn alloy depicted in Fig. 2b displays some refinement of the colonies, aligning with Wang et al.'s [42] observations. However, excessive Sn alloying may reduce ductility; therefore, a limitation of 2 at. % is recommended [41, 43]. Moreover, Fig. 3 shows the XRD spectra for both alloys. The spectra indicate the presence of α_2-Ti$_3$Al and γ-TiAl phases. The alloy without Sn shows intensity at 2θ angles of 38° and 66°, suggesting a higher concentration of γ-TiAl phases. The addition of Sn has resulted in peak shifts and a reduction in the γ-TiAl phase, confirming a distribution of α_2-Ti$_3$Al + γ-TiAl phases. Furthermore, an additional α_2-Ti$_3$Al peak is observed at 2θ = 38° in the Sn-alloyed sample [44].

3.2 Hot corrosion performance of the Ti-48Al-2Nb-0.3Si and Ti-48Al-2Nb-0.3Si-XSn alloys

The cyclic hot corrosion kinetics of the Ti-48Al-2Nb-0.3Si and Ti-48Al-2Nb-0.3Si-1Sn alloys were monitored at 900 °C for 60 h in Na$_2$SO$_4$ + 25 wt.% NaCl salt mixture conducted in air. The weight change per unit area over time

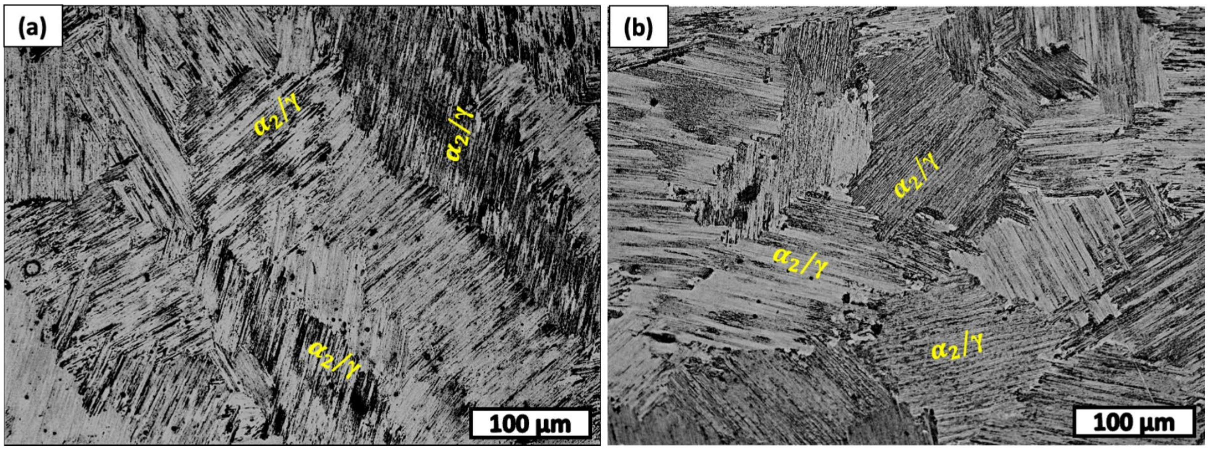

Fig. 2 The optical microscopy micrographs of the a Ti-48Al-2Nb-0.3Si and b Ti-48Al-2Nb-0.3Si-1Sn alloys

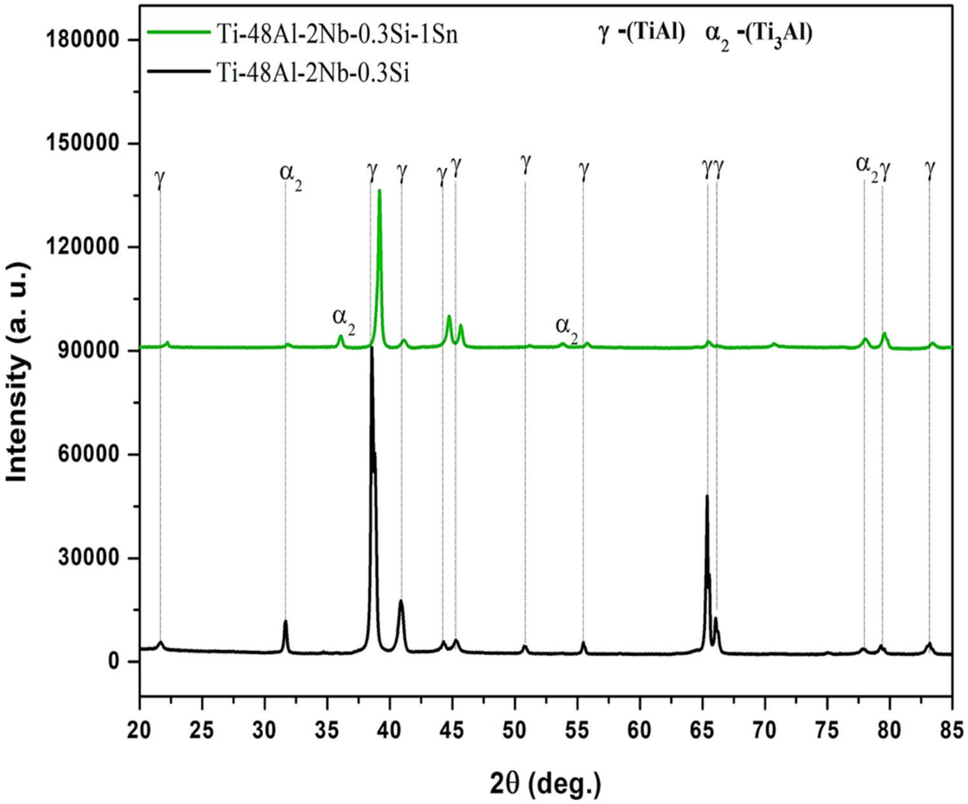

Fig. 3 The XRD patterns for Ti-48Al-2Nb-0.3Si, and Ti-48Al-2Nb-0.3Si-1Sn alloys

was measured to determine the hot corrosion kinetics. Both alloys experienced a hot corrosion attack. The Ti-48Al-2Nb-0.3Si alloy exhibited a severe attack when compared with Ti-48Al-2Nb-0.3Si-1Sn. At 900 °C, above the eutectic point of the $Na_2SO_4 + 25$wt.% NaCl salt mixture [27], the alloys' entire surface was covered by the molten salts, leading to a corrosive attack due to the interaction between the salts and alloys. The cross-sectional morphology of the Ti-48Al-2Nb-0.3Si and Ti-48Al-2Nb-0.3Si-1Sn alloys after cyclic hot corrosion tests is illustrated in Fig. 4a, b. Detailed elemental analysis of the indicated spots in the micrographs was conducted using EDS, and the results are summarised in Table 2. The cross-sectional morphology revealed that both alloys exhibit a light and dark grey multilayer scale

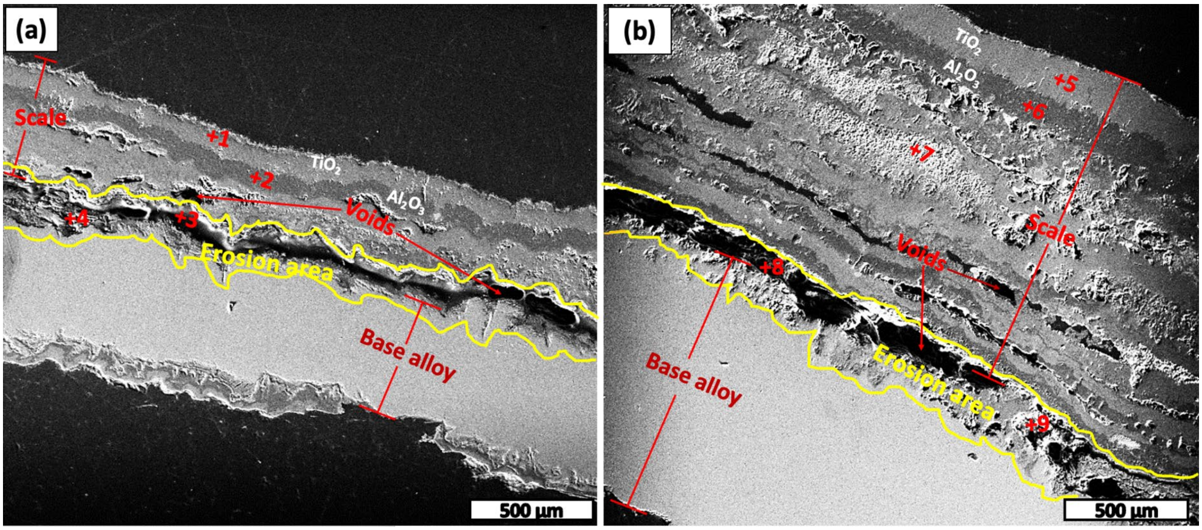

Fig. 4 SEM-SED Cross-sectional images of **a** Ti-48Al-2Nb-0.3Si and **b** Ti-48Al-2Nb-0.3Si-1Sn alloys after 60 h thermal cyclic corrosions

Table 2 The EDS results of the points marked in Fig. 4a, b

Regions (at. %)	Ti	Al	O	Cl	Na	S	Nb	Si	Sn
+1	37.0	-	63.0	-	-	-	-	-	-
+2	2.2	42.9	54.0	0.2	0.4	0.2	-	-	-
+3	1.1	-	71.1	25.5	-	2.3	-	-	-
+4	21.5	3.1	69.1	2.4	-	-	2.8	1.1	-
+5	36.4	-	63.6	-	-	-	-	-	-
+6	3.5	39.7	56.6	0.2	-	-	-	-	-
+7	2.0	-	-	54.8	42.0	1.2	-	-	-
+8	73.6	15.8	-	10.6	-	-	-	-	-
+9	53.4	3.2	35.0	3.7	-	-	0.6	2.7	1.4

indicative of the different oxide layers. However, the scale in Fig. 4b appears thicker (947 µm), indicating the potential resistance of the alloy to hot corrosion compared to that in Fig. 4a with a thinner scale (295 µm). Additionally, the presence of voids within the scale reveals the material degradation or erosion [45]. The localised erosion at the interface of the alloys is indicated by the highlighted space between the alloy and scale.

The EDS spot analysis in Ti-48Al-2Nb-0.3Si and Ti-48Al-2Nb-0.3Si-1Sn alloys showed that the light grey layer contains higher counts of Ti and O, attributable to the presence of TiO_2 [35, 46]. It is represented by spot + 1 (91µm) in Fig. 4a and spot + 5 (146 µm) in Fig. 4b. The dark grey layer indicated by spot + 2 in Fig. 4a and spot + 6 in Fig. 4b exhibited higher Al and O content, signifying the formation of Al_2O_3 [35, 46]. Furthermore, the erosion area is comprised of a mixture of various elements with higher O counts. At the interface, the EDS results in Fig. 4a indicate the presence of O, Cl, and S. The chlorine acted as a catalyst for accelerated corrosion in the corrosion process. Moreover, the sulfidation is evidenced by the presence of sulphur [34]. The EDS results in Fig. 4b show the interface (spot + 8) with high Ti content, followed by Al and Cl due to preferential formation of chlorides [34]. This could potentially be $TiCl_4$, which may act as a catalyst for the corrosion reactions. At the interface (spot + 9), the formation of oxide and chloride phases is evident. However, the concentration of Cl within the alloy matrix is relatively lower compared to the interface.

The change in the mass of Ti-48Al-2Nb-0.3Si and Ti-48Al-2Nb-0.3Si-1Sn alloys over 60 h during cyclic hot corrosion testing is shown in Fig. 5a, b. Initially, the Ti-48Al-2Nb-0.3Si alloy experienced a mass change of -0.73 mg/cm^2, while the Ti-48Al-2Nb-0.3Si-1.0Sn alloy had a mass change of -1.31 mg/cm^2. However, after 18 h of the cyclic corrosion tests, the Ti-48Al-2Nb-0.3Si-1Sn alloy began to gain mass due to the accumulation of corrosion products on its surface. This trend continued throughout the remainder of the tests, although minor debris was observed as displayed in Fig. 5b. In contrast, the spallation on the Ti-48Al-2Nb-0.3Si alloy persisted until the end of the hot corrosion tests. After the 60-h testing period, the Ti-48Al-2Nb-0.3Si alloy exhibited a total weight loss of -51.97 mg/cm^2, while the Ti-48Al-2Nb-0.3Si-1Sn alloy had a weight loss of -17.83 mg/cm^2. These results indicate that the mass loss in the Ti-48Al-2Nb-0.3Si alloy was primarily due to the scale's lack of adhesion to the alloy, as opposed to the Ti-48Al-2Nb-0.3Si-1Sn alloy.

The SEM-SED images in Fig. 6a, b show the morphology of the corrosion products generated on the surface of the TiAl alloys, characterised by a flocculent morphological structure. Figure 6a illustrates the surface morphology of the Ti-48Al-2Nb-0.3Si, which exhibits an elongated crystalline shape structure. In contrast, Fig. 6b exhibits Ti-48Al-2Nb-0.3Si-1Sn, with a thicker flocculent morphology. The TiAl alloys highlight different surface characteristics, indicating variations in the corrosion process and the resulting corrosion products for each alloy composition. The variation between the elongated crystalline needles and the thicker flocculent morphology indicates that the addition of Sn in Ti-48Al-2Nb-0.3Si-1Sn alters the corrosion behaviour.

To gain insights on the composition, elemental analysis was conducted as shown in in Fig. 6a, b. The results of the EDS analysis are summarised in Table 3. The table presents the atomic percentages of different elements present on the surface of Ti-48Al-2Nb-0.3Si in Fig. 6a and Ti-48Al-2Nb-0.3Si-1Sn in Fig. 6b. The surface of the specimens is assumed to consist of TiO_2, due to higher Ti than Al content (Table 3). The EDS analysis on both alloys reveals the presence of additional Na, Cl, and S content, attributable to the un-melted NaCl-Na_2SO_4 salt mixture. Moreover, XRD analysis (Fig. 7) revealed that the corrosion products present in the oxide scales were Na_2TiO_3, $NaAlO_2$, and $NaTi_5NbO_{13}$, with TiO_2 and Al_2O_3. However, when comparing the Ti-48Al-2Nb-0.3Si-1Sn alloy to the Ti-48Al-2Nb-0.3Si alloy, the Ti-48Al-2Nb-0.3Si-1Sn alloy showed the presence of new peaks, indicating the formation of additional compounds in its oxide scales which corresponds to SnO_2 and SiO_2. The presence of these oxides indicates that elements from the alloy have reacted with oxygen to form oxides during the hot corrosion process. Even though the

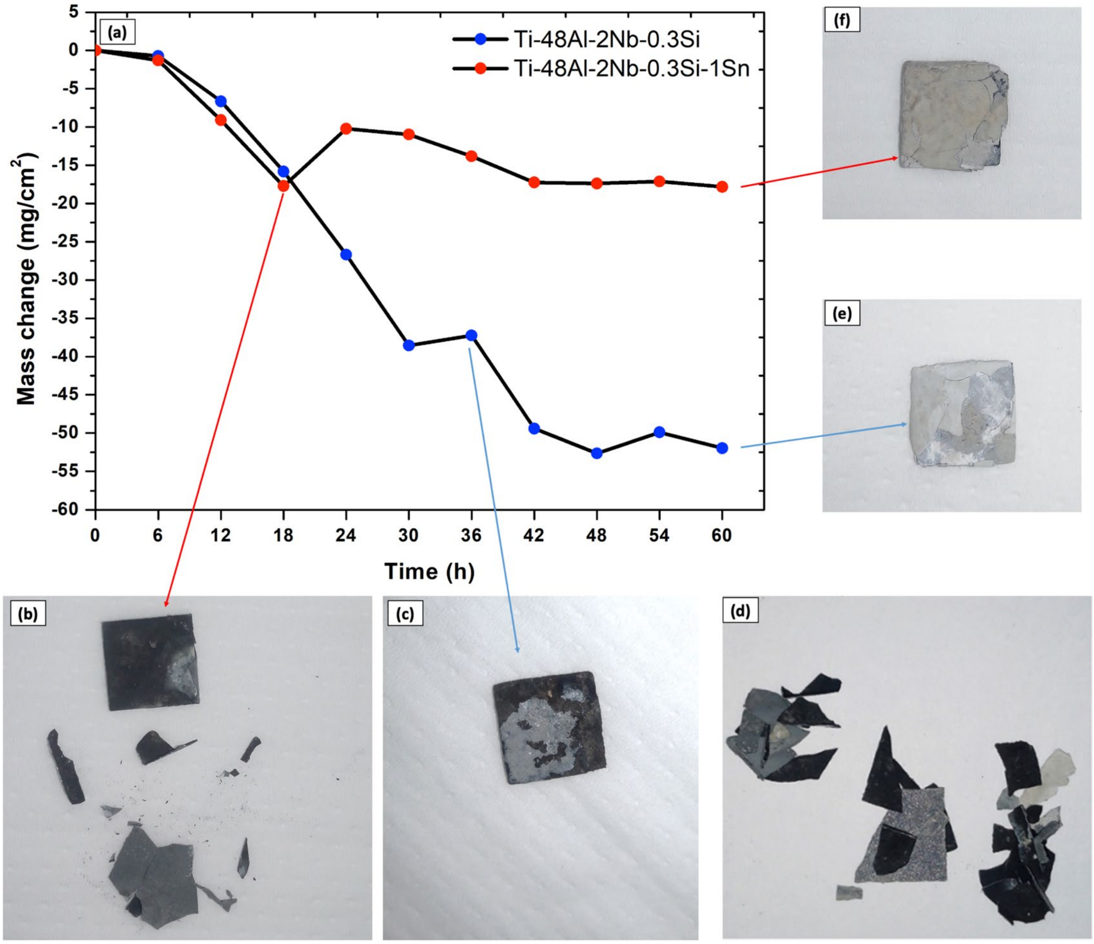

Fig. 5 **a** Mass change curves of Ti-48Al-2Nb-0.3Si and Ti-48Al-2Nb-0.3Si-1Sn alloys over 60 h of cyclic hot corrosion testing. **b–f** Macrographs showing spallation and oxide scaling on the surfaces of the Ti-48Al-2Nb-0.3Si/1Sn alloys

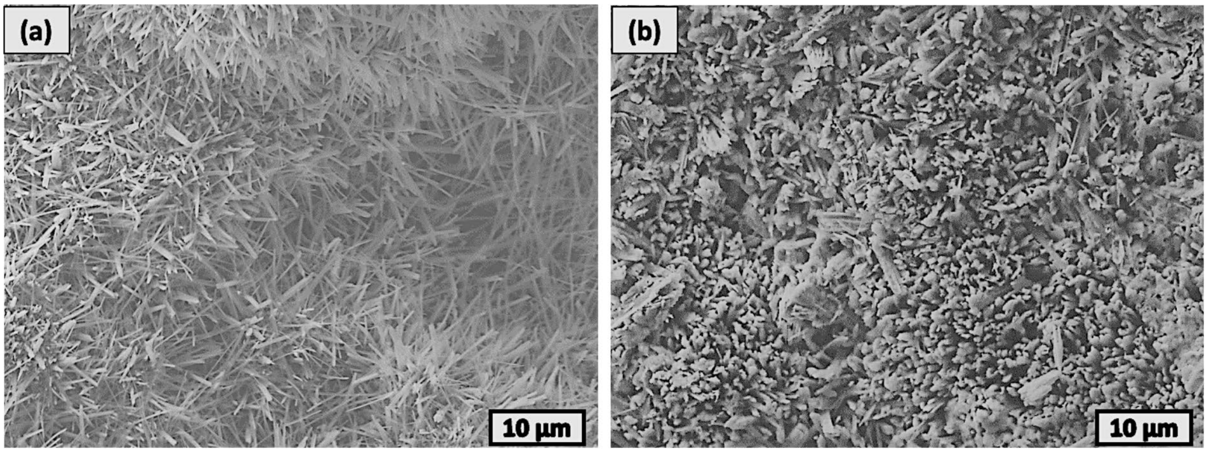

Fig. 6 SEM-secondary electron detector (SED) images of the **a** Ti-48Al-2Nb-0.3Si and **b** Ti-48Al-2Nb-0.3S-1Sn alloys after 60 h thermal cyclic corrosions

Table 3 The EDS surface analysis of the specimen in Fig. 2a, b

Elements (at. %)	Ti-48Al-2Nb-0.3Si	Ti-48Al-2Nb-0.3Si-1.0Sn
Ti	26.7	24.6
Al	0.9	0.2
O	61.6	56.1
Na	09.0	11.0
Cl	1.0	7.8
S	0.8	0.4

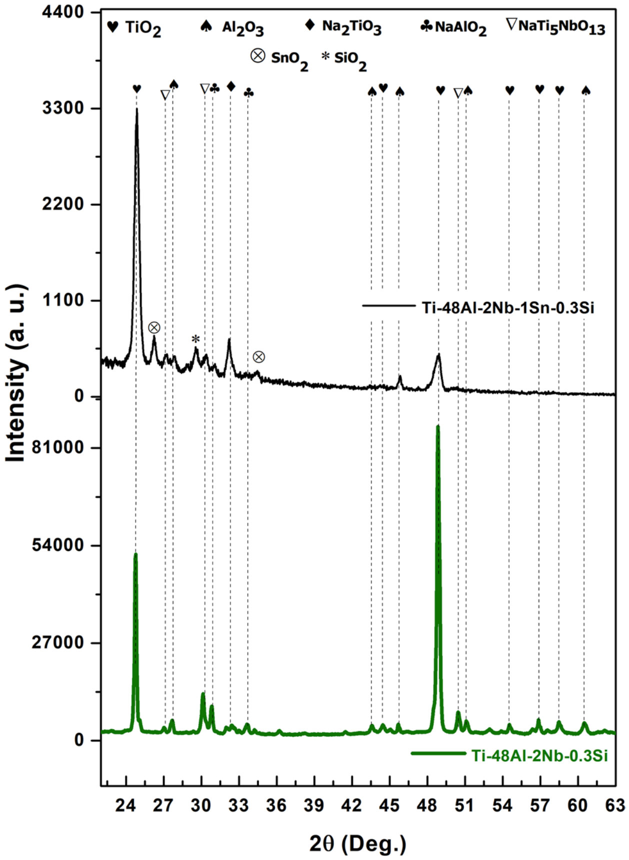

Fig. 7 XRD patterns of the Ti-48Al-2Nb-0.3Si and Ti-48Al-2Nb-0.3Si-1Sn alloys after cyclic hot corrosion for 60 h at 900 °C

Si was detected by EDS in the Ti-48Al-2Nb-0.3Si alloy, XRD technique was unable to detect it due to low levels. The additional compounds of SnO_2 and SiO_2, in the oxide scales of the Ti-48Al-2Nb-0.3Si-1Sn, indicate that the presence of Sn and Si influences the hot corrosion behaviour and the resulting oxide scale composition in comparison to the Ti-48Al-2Nb-0.3Si alloy.

The corrosion scale of the Ti-48Al-2Nb-0.3Si-1Sn alloy is shown in Fig. 8a. To investigate the intermixing of the corrosion media and the alloy at the end of the 60-h thermal cyclic corrosion testing, an EDS elemental analysis of the corrosion scale illustrated in Fig. 8c was performed. The crystal lattice planes of the TiO_2 anatase with a d-spacing of 0.31 nm for the (101) plane are shown in Fig. 9a. Its selected area electron diffraction (SAED) pattern for the anatase phase of TiO_2 is shown in Fig. 9b. The HRTEM results align well with the XRD analysis presented in Fig. 7. These results exhibit a prominent diffraction peak at $2\theta = 25.2°$, indicating a significant presence of anatase TiO_2 phase [46]. Anatase is a stable phase of TiO_2 at room temperature, existing in a tetragonal crystal structure, and transforms into rutile at high temperature [48].

Figure 10a shows the salt deposits such as NaCl and Na_2SO_4 on the surface of alloys exposed to an oxidising atmosphere to generate accelerated corrosion [2, 34–36, 39, 45, 50–52]. The corrosion process is attributable to the high reactivity of Ti and Al with chlorine agents present in NaCl penetrating the surface of the alloy through grain boundaries or defects in the microstructure, reaching the alloy's matrix [53, 54]. The reactivity between Ti, Al, and Cl results in the generation of gaseous species, which penetrates the material [34]. Consequently, these gaseous species disrupt the protective scale on the alloy's surface. As the alloys undergo self-sustaining reactions in the presence of NaCl, the corrosion process is accelerated. This acceleration of corrosion can lead to mechanical stress and induce cracks and spalling [35, 36].

The reactive elements present in the alloy, such as Ti and Al, react with the O_2 in the surrounding air leading to the formation of metal oxides, such as TiO_2 and Al_2O_3. The formation of these metal oxides plays a crucial role in providing a protective layer against corrosion, preventing further degradation of the alloy and helping to maintain its integrity. Figure 10b illustrates the hot corrosion mechanism within the Ti-48Al-2Nb-0.3Si/1Sn alloy under a molten NaCl-Na_2SO_4 salt mixture. The mechanism involves several reactions between the medium salts, the oxides, and the alloy. Figure 10c illustrates the specimen after hot corrosion, where this phenomenon is observed as erosion area at the interface of the alloy and the multilayer scale. Pulverisation, the breaking down of the scale into fine particles, detaches from the alloy surface and exposes it to further corrosion [52]. This process can occur due to various factors, including stress accumulation, differential expansion, and contraction, as well as the diffusion of reactive species [36–43, 50].

- At high temperatures, the salt mixture dissociates into Na^+, Cl^-, and SO_4^{2-} ions (Eqs. 2 and 3). These ions penetrate the alloy surface through the protective scale.
- The Cl^- ions react with the protective scale, such as TiO_2 and Al_2O_3, resulting in the formation of volatile Cl_2 gas (Eqs. 4 and 5).

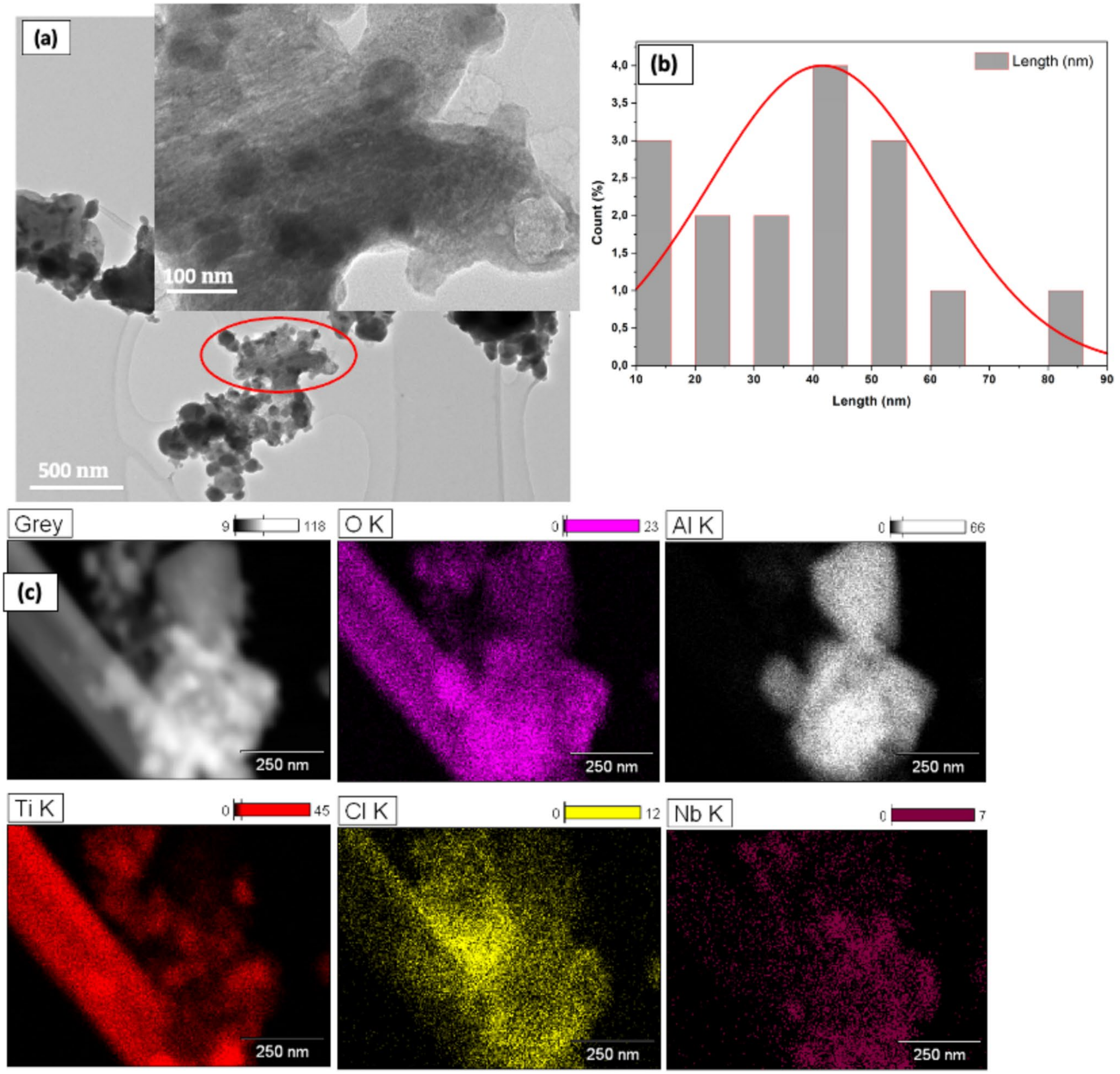

Fig. 8 TEM images of the corroded scale of Ti-48Al-2Nb-0.3Si-1Sn alloy after 60 h thermal cycling; **a** corroded scale of the alloy, **b** particle size distribution, **c** elemental mapping of the (O, Cl, Ti, Al, Nb) interaction between alloy and corrosion medium

- The Na^+ ions react with alloy elements like Ti, Al, and Nb, forming oxides such as $NaTi_5NbO_{13}$, $NaAlO_2$, and Na_2TiO_3 (Eq. 6).
- The Cl_2 gas reacts with the alloy elements, forming metal chlorides (MCl_x) like $TiCl_4$ and $AlCl_3$ (Eqs. 7, 8, and 9).
- The metal chlorides then react with O_2, forming oxides and releasing more Cl_2 gas (Eqs. 10, 11, and 12).

These reactions contribute to the deterioration of the alloy surface due to the formation of volatile gases (Cl_2), metal chlorides (MCl_x), and metal oxides (MO_x). The release of Cl_2 gas creates a continuous cycle of corrosion as it reacts with the protective scale and alloy elements, further degrading the surface. These reactions are self-sustaining and accelerate the corrosion of the alloy by breaking down the protective oxide layer. This causes damage to the alloy through grain boundaries or defects in the microstructure, reaching the underlying material and leading to further degradation and pulverisation. The following equations show the reactions involved in the hot

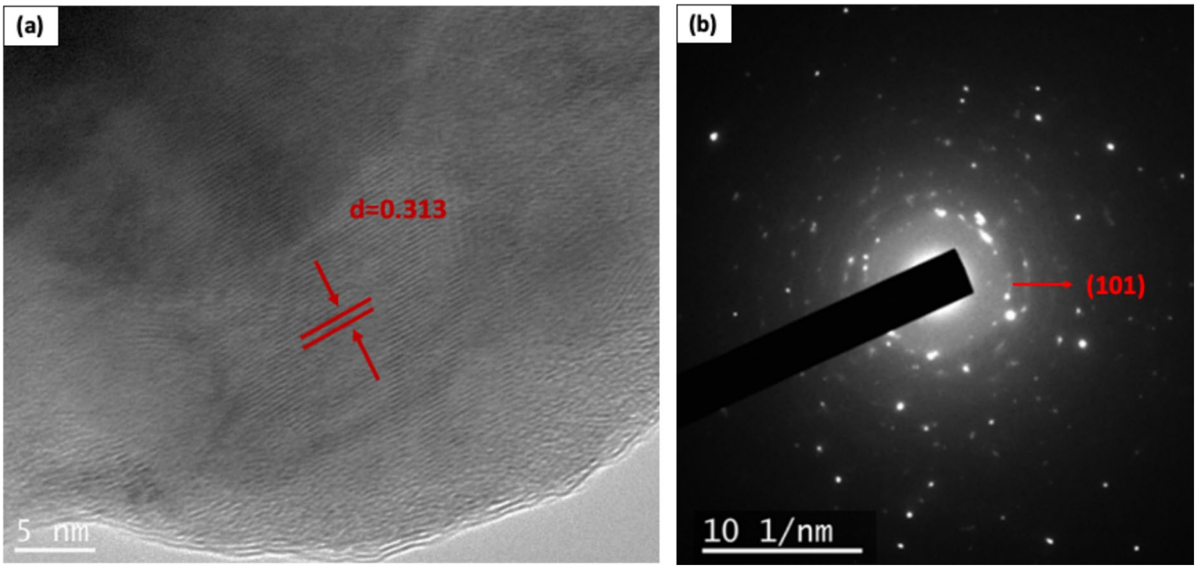

Fig. 9 TEM images of the corroded scale of Ti-48Al-2Nb-0.3Si-1Sn alloy after 60 h thermal cycling. **a** HRTEM indicating the anatase TiO_2. **b** SAED pattern of corrosion scale

corrosion mechanism between TiAl and NaCl-Na_2SO_4 hot salts [34, 36, 52]:

$$NaCl \rightarrow Na^+ + Cl^- \quad (2)$$

$$Na_2SO_4 \rightarrow 2Na^+ + SO_4{}^{2-} \quad (3)$$

$$4NaCl + 2Al_2O_3 + O_2 \rightarrow 4NaAlO_2 + 2Cl_2 \quad (4)$$

$$4NaCl + 2TiO_2 + O_2 \rightarrow 2Na_2TiO_3 + 2Cl_2 \quad (5)$$

$$Na_2O + 10TiO_2 + Nb_2O_5 \rightarrow 2NaTi_5NbO_{13} \quad (6)$$

$$Ti + Cl_2 \rightarrow TiCl_2 \quad (7)$$

$$Ti + 2Cl_2 \rightarrow TiCl_4 \quad (8)$$

$$2Al + 3Cl_2 \rightarrow 2AlCl_3 \quad (9)$$

$$TiCl_2 + O_2 \rightarrow TiO_2 + Cl_2 \quad (10)$$

$$TiCl_4 + O_2 \rightarrow TiO_2 + 2Cl_2 \quad (11)$$

$$4AlCl_3 + 3O_2 \rightarrow 2Al_2O_3 + 6Cl_2 \quad (12)$$

$$2Na_2SO_4 + 4Ti \rightarrow 2Na_2TiO_3 + TiS_2 + O_2 \quad (13)$$

It is evident that the spallation or accelerated mass loss from the Ti-48Al-2Nb-0.3Si alloy can be attributed to the process of pulverisation. The multilayer scale consists of different oxide layers, such as TiO_2 and Al_2O_3, which have different thermal expansion coefficients from the underlying alloy. During high-temperature service and exposure to corrosive environments, these oxides cause stress to build up at the interface, leading to cracking and pulverisation of the scale [52]. The multilayer scale and the underlying alloy experience different degrees of expansion and contraction during thermal cycling in high-temperature environments. This results into cyclic thermal stress at the interface, weakening the bond between the scale and the alloy and making them prone to pulverisation [52]. Corrosive gases, such as SO_2 and Cl_2, can diffuse through the scale and react with the alloy or the scale constituents. This can result in the formation of compounds that have different physical properties from the Ti-48Al-2Nb-0.3Si/1Sn, such as metal sulphides and chlorides. These differences contribute to pulverisation at the interface [34–36]. The presence of sulfidation at the interface of Ti-48Al-2Nb-0.3Si-1Sn might as well have influenced the spallation. This combination led to the formation of compounds with physical properties that differ from Ti–Al-Nb-Si-xSn, such as metal sulphides and chlorides, contributing to interface pulverisation [34].

3.3 Mechanical properties

The mechanical properties of the Ti-48Al-2Nb-0.3Si-1Sn and Ti-48Al-2Nb-0.3Si alloys were evaluated before and after conducting hot corrosion tests. Figure 11a shows the yield stress (YS), ultimate tensile stress (UTS), and elongation (%El) before the cyclic hot corrosion test. The YS of

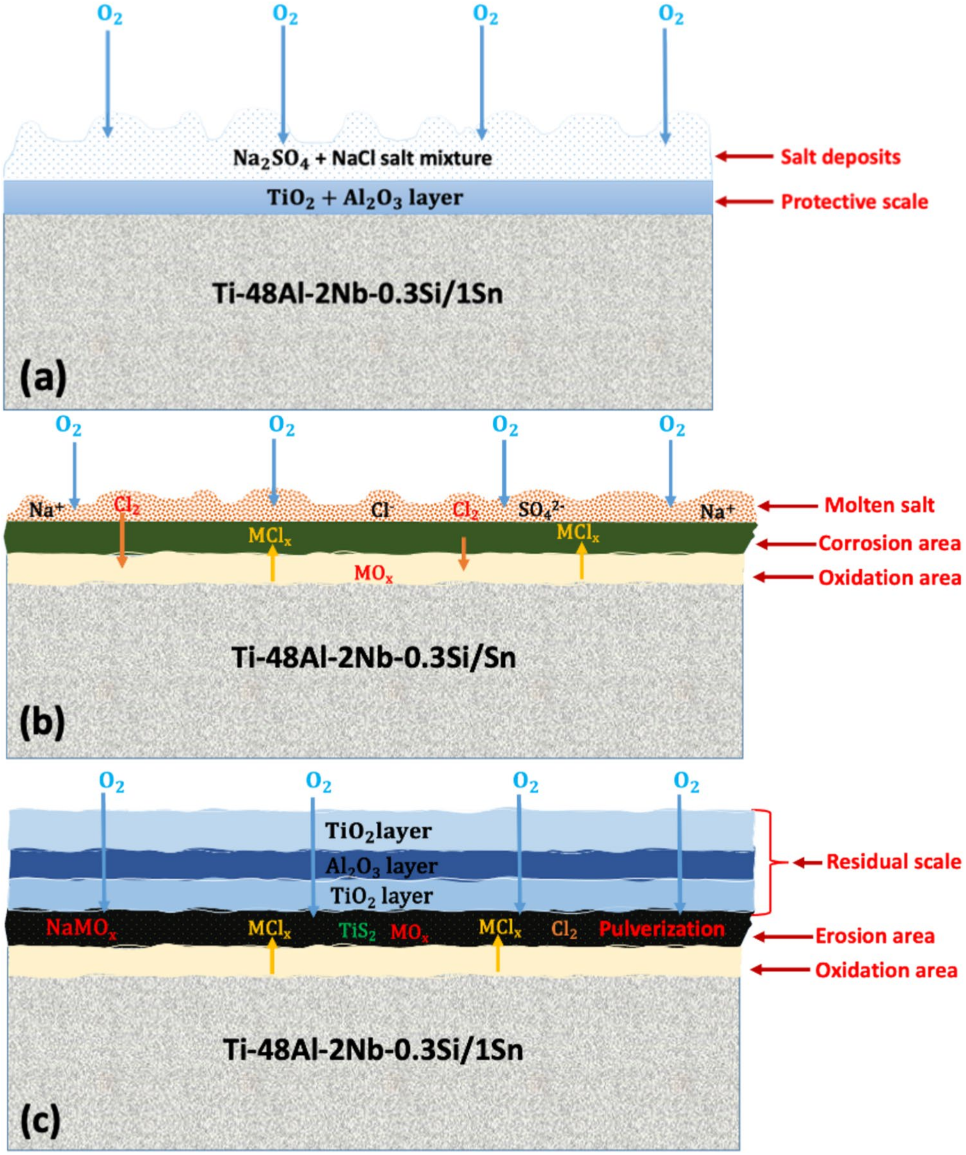

Fig. 10 Schematic illustrations of hot corrosion mechanisms of Ti-48Al-2Nb-0.3Si/1Sn induced by NaCl-Na_2SO_4 salt mixture. **a** Initial deposition of the salt mixture onto the substrate surface. **b** Liquefaction of the salt mixture leading to the initiation of the hot corrosion process. **c** Impact of hot corrosion on the sample post-processing, highlighting the morphological and compositional changes observed

Ti-48Al-2Nb-0.3Si alloy is 451 MPa, UTS of 470 MPa, and %El of 2.0%. On the other hand, the Ti-48Al-2Nb-0.3Si-1Sn alloy exhibited YS of 307 MPa, UTS of 485 MPa, with %El of 2.2%. The higher YS and UTS values of the Ti-48Al-2Nb-0.3Si alloy are indicative of higher strength when compared to the Ti-48Al-2Nb-0.3Si-1Sn alloy.

Figure 11b shows the hot corrosion tests of the Ti-48Al-2Nb-0.3Si and Ti-48Al-2Nb-0.3Si-1Sn alloys after the cyclic hot corrosion test. The results show that corrosion influenced the mechanical properties of both alloys. The YS (318 MPa), UTS (418 MPa), and %El (1.7) of Ti-48Al-2Nb-0.3Si alloys have decreased. On the other hand, the Ti-48Al-2Nb-0.3Si-1Sn alloy exhibited a lower YS (257 MPa) and increased UTS (479 MPa). The %El for this alloy decreased to 2.0%. The results indicate that the cyclic hot corrosion tests significantly affected the mechanical properties. However, Ti-48Al-2Nb-0.3Si-1Sn was less affected when compared to Ti-48Al-2Nb-0.3Si alloy. The corrosion-induced localised surface defects have influenced the initiation of cracks during loading, leading to the reduction in mechanical properties.

Figure 12 shows the hardness test results. The micro-hardness results of the Ti-48Al-2Nb-0.3Si before the hot corrosion test were measured 299 HV and decreased to 290 after the cyclic hot corrosion test. The Ti-48Al-2Nb-0.3Si-1Sn alloy hardness before the cyclic hot corrosion test was 280 HV and decreased to 263 HV after the cyclic hot corrosion test. The micro-hardness results indicate that both alloys experienced a decrease in hardness after the cyclic hot corrosion test. These results emphasise the importance of considering the potential effects of hot corrosion on the mechanical properties of Ti-48Al-2Nb-0.3Si and Ti-48Al-2Nb-0.3-1Sn

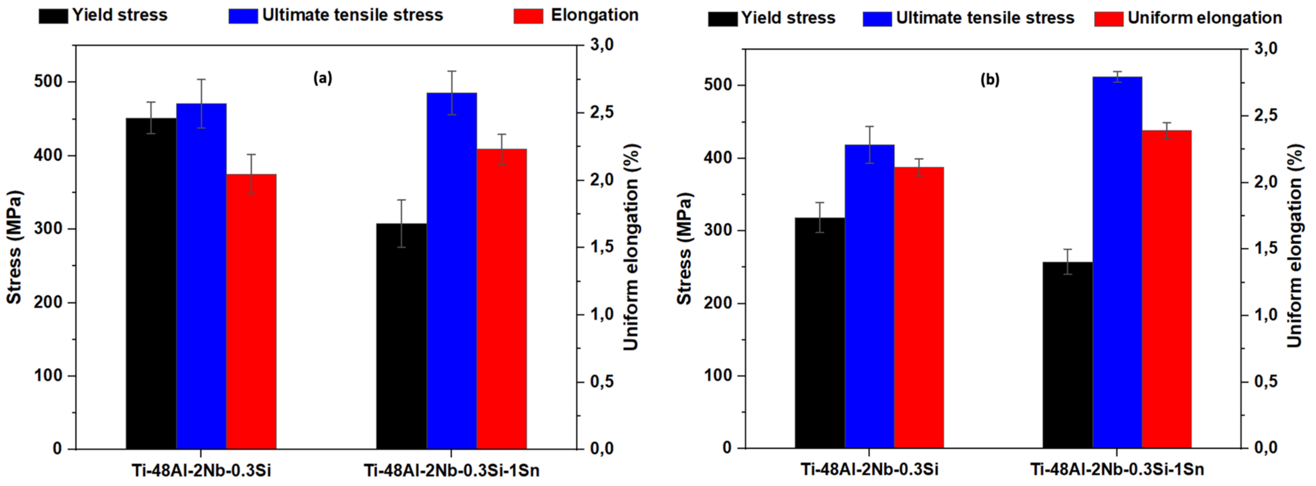

Fig. 11 Compression engineering yield stress-ultimate tensile stress results of Ti-48Al-2Nb-0Sn-0.3Si and Ti-48Al-2Nb-0.3Si-1Sn alloys, **a** before the cyclic hot corrosion test and **b** after the cyclic hot corrosion test

Fig. 12 Vickers hardness of Ti-48Al-2Nb-0.3Si and Ti-48Al-2Nb-0.3-1Sn before and after cyclic hot corrosion tests

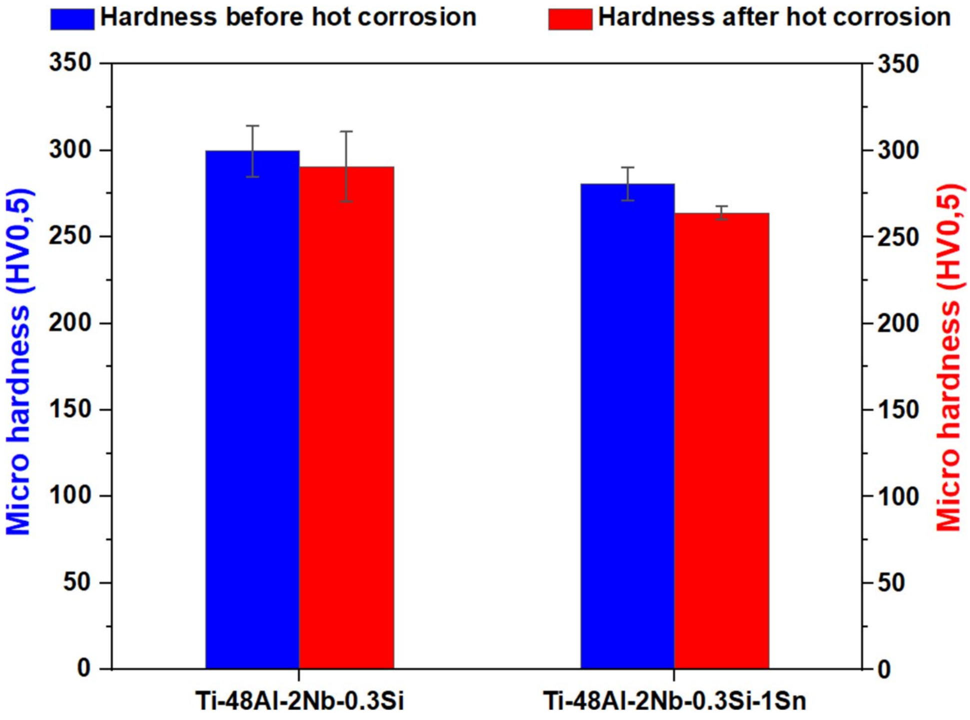

alloys when evaluating their suitability for high-temperature applications.

4 Conclusion

The current study investigated the hot corrosion behaviour of Ti-48Al-2Nb-0.3Si and Ti-48Al-2Nb-0.3Si-1Sn alloys under NaCl and Na_2SO_4 salt deposits at 900 °C. Both alloys were subjected to a hot corrosion attack; however, the Ti-48Al-2Nb-0.3Si-1Sn alloy demonstrated better corrosion resistance. The following are the findings:

- The Sn addition promoted the formation of a SnO_2 layer on the alloy surface, which acted as a barrier against the penetration of corrosive salts into the alloy. The Sn addition also enhanced the adhesion and cohesion of the Al_2O_3 scale, which prevented spallation and cracking.
- The hot corrosion mechanisms in Ti-48Al-2Nb-0.3Si and Ti-48Al-2Nb-0.3Si-1Sn alloys involved a combination of oxidation, sodium, and chlorine-induced corro-

sion processes. The formation of complex multi-layered oxide scales, consisting of TiO_2, Al_2O_3, and the interaction between the alloy and the aggressive environment were crucial factors in determining the overall corrosion behaviour.

- The short cyclic loading had a more detrimental impact on mass loss than long-time cyclic loading. This was because short cyclic loading exposed the alloy to frequent thermal shocks and stresses, which damaged the protective oxide layer and accelerated the corrosion process.

Therefore, this study concluded that Sn is an effective alloying element for enhancing corrosion resistance of TiAl-based alloys.

Acknowledgements The Thuthuka National Research Foundation (grant no. 138314) is acknowledged for funding this work. Additionally, many thanks should go to the Council of Scientific and Industrial Research (CSIR) as well as the University of Pretoria (UP) in the Republic of South Africa for providing laboratory equipment.

Author contribution Steven Magogodi: conceptualization, methodology, and writing—original draft. Maria N. Mathabathe: writing—review and editing, funding acquisition, and supervision. C. W. Siyasiya: supervision and review and editing. Amogelang S. Bolokang: supervision and writing—review and editing. V. N. Vilane: data curation, methodology, and formal analysis. R. Rikhotso-Mbungela: data curation, methodology, and formal analysis.

Funding Open access funding provided by Council for Scientific and Industrial Research.

Data availability The raw/processed data required to reproduce these findings cannot be shared at this time as the data also forms part of an ongoing study.

Declarations

Competing interests The authors declare no competing interests.

Open Access This article is licensed under a Creative Commons Attribution 4.0 International License, which permits use, sharing, adaptation, distribution and reproduction in any medium or format, as long as you give appropriate credit to the original author(s) and the source, provide a link to the Creative Commons licence, and indicate if changes were made. The images or other third party material in this article are included in the article's Creative Commons licence, unless indicated otherwise in a credit line to the material. If material is not included in the article's Creative Commons licence and your intended use is not permitted by statutory regulation or exceeds the permitted use, you will need to obtain permission directly from the copyright holder. To view a copy of this licence, visit http://creativecommons.org/licenses/by/4.0/.

References

1. Wu L, Wu W, Song J, Hou G, Cao H, Tang Y (2018) Enhanced high temperature oxidation resistance for γ -TiAl alloy with electrodeposited SiO_2 film. Corros Sci 140:388–401
2. Garip Y, Ozdemir O (2019) Comparative study of the oxidation and hot corrosion behaviours of TiAl-Cr intermetallic alloy produced by electric current activated sintering. J Alloys Compd 780:364–377
3. Clemens H, Smarsly W (2011) Light-weight intermetallic titanium aluminides – status of research and development. Adv Mater Res 278:551–556
4. Appel BF, Brossmann Ulrich, Christoph Ulrich, Eggert Stefan, Janschek Peter, Lorenz Uwe, Müllauer Johann, Oehring Michael, Paul Jonathan D. H (2000) Recent progress in the development of gamma titanium aluminide alloys. Adv Eng Mater 2(11):699–720
5. Wu X (2006) Review of alloy and process development of TiAl alloys. Intermetallics 14:1114–1122
6. Sun Z, Wu W, Chen Y, Yuan Z, Zhang Y (2020) "Microstructure characterization and hot corrosion mechanism of as-cast and heat treated high Nb containing TiAl alloy. Corros Sci 185:109399
7. Nochovnaya NA, Panin PV, Kochetkov AS, Bokov KA (2014) Modern refractory alloys based on titanium gamma-aluminide: prospects of development and application. Met Sci Heat Treat 56(7–8):364–367
8. Clemens H, Bartels A, Bystrzanowski S, Chladil H, Leitner H, Dehm G, Gerling R, Schimansky FP (2006) Grain refinement in γ-TiAl-based alloys by solid state phase transformations. Intermetallics 14(12):1380–1385. https://doi.org/10.1016/j.intermet.2005.11.015
9. Saage H, Huang AJ, Hu D, Loretto MH, Wu X (2009) Microstructures and tensile properties of massively transformed and aged Ti46Al8Nb and Ti46Al8Ta alloys. Intermetallics 17(1–2):32–38
10. Hu D, Huang AJ, Wu X (2007) On the massive phase transformation regime in TiAl alloys: the alloying effect on massive / lamellar competition. Intermetallics 15(2007):327–332
11. Klein T, Rashkova B, Holec D, Clemens H, Mayer S (2016) Silicon distribution and silicide precipitation during annealing in an advanced multi-phase Ɣ -TiAl based alloy. Acta Mater 110:236–245
12. Liu B, Liu Y (2015) Powder metallurgy titanium aluminide alloys. Sci Technol Applic 515–531. https://doi.org/10.1016/B978-0-12-800054-0.00027-7
13. Mall JH, Mctiernan BJ (2000) PM TiAl alloys : the sky's the limit. Met Powder Rep 55(1):18–22
14. Gerling BR, Clemens H, Schimansky FP (2004) Power metallurgical processing of intermetallic gamma titanium aluminides. Adv Eng Mater 6(1–2):23–38
15 Kothari K, Radhakrishnan R, Wereley NM, Sudarshan TS (2013) Microstructure and mechanical properties of consolidated gamma titanium aluminides. Powder Metall 50(1):20–27
16. Danninger H, Gierl-Mayer C (2013) Advanced powder metallurgy steel alloys. Adv Powder Metall 7:149–198
17. Qian M (2010) Cold compaction and sintering of titanium and its alloys for near-net-shape or preform fabrication. Int J Pow Metall 46(5):29–44
18. Cominotti RÃ, Gentili E (2008) Near net shape technology: an innovative opportunity for the automotive industry. Robot Comput-Integr Manuf 24:722–727
19. Camagu ST, Mathabathe NM, Motaung DE, Muller TFG, Arendse CJ, Bolokang AS (2019) Investigation into the thermal behaviour of the B2–NiAl intermetallic alloy produced by compaction and sintering of the elemental Ni and Al powders. Vacuum 169:108
20. Couret A, Molénat G, Galy J, Thomas M (2008) Microstructures and mechanical properties of TiAl alloys consolidated by spark plasma sintering. Intermetallics 16(9):1134–1141. https://doi.org/10.1016/j.intermet.2008.06.015
21. Mathabathe MN, Bolokang AS, Govender G, Siyasiya CW, Mostert RJ (2019) Cold-pressing and vacuum arc melting of Ɣ -TiAl based alloys. Adv Powder Technol 30(12):2925–2939

22. Jiang XJ, Zhang YY, Yang N, Wang SQ, Ran QX (2020) "The effect of 3 wt % oxygen on mechanical properties of a TiZrAl alloy prepared by vacuum arc melting. Vacuum 175:109248
23. Stephen MS, Brookes P (2006) Thermo-mechanical fatigue behaviour of the near-γ-titanium aluminide alloy TNB-V5 under uniaxial and multiaxial loading. Scr Mater 54(2):137–141
24. Noda T (1998) Application of cast gamma TiAl for automobiles. Intermetallics 6(7–8):709–713
25. Brotzu A, Felli F, Pilone D (2014) Intermetallics Effect of alloying elements on the behaviour of TiAl-based alloys. Intermetallics 54:176–180
26. Ostrovskaya O, Badini C, Baudana G, Padovano E, Biamino S (2018) Intermetallics thermogravimetric investigation on oxidation kinetics of complex Ti-Al alloys. Intermetallics 93:244–250
27. Jiang Y, Sun Y, Jacob RD, Bruno F, Li S (2018) Novel Na2SO4-NaCl-ceramic composites as high temperature phase change materials for solar thermal power plants (Part I). Solar Ener Mater Solar Cells 178:74–83
28. Chou K, Arbor A, Marquis EA (2018) Early oxidation behavior of Si-coated titanium. Corros Sci 140:297–306
29. Lee J, Park H, Kim J, Jang J, Hong S (2020) Constitutive behavior and microstructural evolution in Ti – Al – Si ternary alloys processed by mechanical milling and spark plasma sintering. Integrative Med Res 9(2):2247–2258
30. Knaislová A, Novák P, Průša F, Cabibbo M, Jaworska L, Vojtěch D (2019) High-temperature oxidation of Ti–Al–Si alloys prepared by powder metallurgy. J Alloys Compd 810:151895
31. Noda T, Okabe M, Isobea S, Sayashib M (1995) Creep silicide precipitation strengthened TiAl. Mater Sci Eng A 192–193:774–779
32. Tsuyama S, Mitao S, Minakawa K (1992) Alloy modification of y-base titanium aluminide for improved oxidation resistance, creep strength and fracture toughness. Mater Sci Eng A 153(1–2):451–456
33. Pan Y, Lu X, Hayat MD, Yang F, Liu CC, Li Y, Li XY, Xu W, Qu XH, Cao P (2020) Effect of Sn addition on the high-temperature oxidation behavior of high Nb-containing TiAl alloys. Corros Sci 166:108449
34 Mitoraj-królikowska M, Godlewska E (2017) Hot corrosion behaviour of (γ+α2)-Ti-46Al-8Nb (at.%) and α-Ti-6Al-1Mn (at.%) alloys. Corros Sci 115:18–29
35. Tang Z, Wang F, Wu W (1999) Hot-corrosion behavior of TiAl-base intermetallics in molten salts. Oxid Met 51:235–250
36 Zhang K, Li Z, Gao W (2002) Hot corrosion behaviour of Ti – Al based intermetallics. Mater Lett 57:834–843
37. Tang Z, Wang F, Wu W (1999) Effect of a sputtered TiAlCr coating on hot corrosion resistance of gamma-TiAl. Intermetallics 7(11):1271–1274
38 Ellard JJM, Mathabathe MN, Siyasiya CW, Bolokang AS (2023) Vacuum melting of compressed powders and hot rolling of the as-cast Ti-48Al-2Nb-0.7 Cr-0.3 Si intermetallic alloy: mechanical properties and microstructural analysis. J Manuf Proc 101:1214–1223
39. Mathabathe MN, Govender S, Bolokang AS, Mostert RJ (2018) Phase transformation and microstructural control of the α-solidifying γ-Ti-45Al-2Nb-0.7Cr-0.3Si intermetallic alloy. J Alloys Compd 757:8–15
40. Ellard JJ, Mathabathe MN, Siyasiya CW, Bolokang AS (2022) Powder characteristics blending, and microstructural analysis of a hot-pack rolled vacuum arc-melted γ-tial-based sheet. S Afr J Ind Eng 33(3):274–283
41. Pan Y, Lu X, Liu C, Hui T, Zhang C, Qu X (2020) Sintering densification, microstructure and mechanical properties of Sn-doped high Nb-containing TiAl alloys fabricated by pressureless sintering. Intermetallics 125:106891
42. Wang DN, Inui H, Lin D, Yamaguchi M (1996) Effects of Sn additions on the microstructures and tensile properties of two-phase TiAl alloys. Intermetallics 4(3):191–200
43. Zhang C, Zhang S, Pan Y, Xu W, Singh HP, Liu B, Lu D, Wang H, Zhang J, Lu X (2022) Effect of Sn addition on the mechanical properties and high-temperature oxidation resistance of intermetallic TiAl alloys by first principles study and experimental investigation. J Mater Res Technol 21:3666–3677
44. Bolokang AS, Mathabathe MN, Chikosha S, Motaung DE (2020) Investigating the heat resistant properties of the TiNi shape memory alloy on the B19'→ B2 phase transformation using the alloy powder. J Surf Interf 20:100608
45. Wei Z, Li X, Lv W, Ming B, Li Y, Liu X, Lai S, Liu F (2023) Structure and hot corrosion behavior of an Al-Co-Y Co-deposited coating on TiAl alloy. J Mater Eng Perf 32(11):4796–4806
46. Pilone D, Mondal A, Zortea L (2022) High-temperature oxidation behaviour of a TiAl-based alloy subjected to aluminium hot-dipping. Oxid Met 98(5–6):529–543
47. Wang K, Zhuo Y, Chen J, Gao D, Ren Y, Wang C, Qi Z (2020) Crystalline phase regulation of anatase–rutile TiO_2 for the enhancement of photocatalytic activity. RSC Adv 10(71):43592–43598
48. Cavalheiro AA, De Oliveira LCS, dos Santos SAL (2017) Structural aspects of anatase to rutile phase transition in titanium dioxide powders elucidated by the Rietveld method. *Titanium Dioxide*, 63. Mater Sci. https://doi.org/10.5772/intechopen.68601
49. Eliaz N, Shemesh G, Latanision RM (2002) Hot corrosion in gas turbine components. Eng Fail Anal 9(1):31–43
50. Dai J, Zhang H, Sun C, Li S, Chen C, Yang Y (2020) The effect of Nb and Si on the hot corrosion behaviors of TiAl coatings on a Ti-6Al-4V alloy. Corros Sci 168:108578
51. Qiao Y, Kong J, Guo X (2018) Hot corrosion phenomena of Nb-Ti-Si based alloy and its silicide coating induced by different corrosive environments at 900° C. Ceram Int 44(7):7978–7990
52. Qiao Y, Kong J, Guo X (2018) Hot corrosion phenomena of Nb-Ti-Si based alloy and its silicide coating induced by different corrosive environments at 900° C. Ceram Int 44(7):7978–7990
53. Kanyane LR, Popoola AP, Pityana S, Tlotleng M (2022) Heat-treatment effect on anti-corrosion behaviour and tribological properties of LENS in-situ synthesized titanium aluminide. Int J Lightweight Mater Manuf 5(2):153–161

Publisher's Note Springer Nature remains neutral with regard to jurisdictional claims in published maps and institutional affiliations.